Supplementary file: 3D micro-devices for enhancing the lateral resolution in optical microscopy

Gordon Zyla[1] *, Göran Maconi[2], Anton Nolvi[2], Jan Marx[3], Dimitra Ladika[1], Ari Salmi[2], Vasileia Melissinaki[1], Ivan Kassamakov[2], and Maria Farsari[1]

[1]*Institute of Electronic Structure and Laser, Foundation for Research and Technology-Hellas, Heraklion, Greece*
[2]*Electronics Research Laboratory, Department of Physics, University of Helsinki, Helsinki, Finland*
[3]*Applied Laser Technologies, Ruhr University Bochum, Bochum, Germany*
*Correspondence to: Gordon Zyla: zyla@iesl.forth.gr

Preparation and handling of hybrid material with Zr-based inorganic component

The photosensitive material used for multi-photon lithography (MPL) in the present research is a hybrid of organic and Zr-based inorganic photopolymer. It was in-housely synthesized at IESL-FORTH (Institute of Electronic Structure and Laser, Foundation for Research and Technology-Hellas). The photopolymer comprises two organic photopolymerizable monomers: Methacryloxypropyl trimethoxysilane (MAPTMS, 99%, Sigma-Aldrich, Germany) and 2-(dimethylamino) ethyl methacrylate (DMAEMA, 98%, Sigma-Aldrich, Germany). These components form an inorganic network via Zirconium n-propoxide (ZPO, 70%, Sigma-Aldrich, Germany) and the alkoxysilane groups present in MAPTMS. The composition of this resist closely mirrors the well-known MPL-material SZ2080[TM] [1]. Given the quenching ability of DMAEMA [2, 3], this photoresist provides minimal shrinkage and high resolution in MPL, thus achieving high-quality processing results.

The material was prepared using a sol-gel process. Initially, MAPTMS was hydrolyzed using an HCl solution (0.1 M). Afterwards, ZPO was incorporated into the hydrolyzed MAPTMS at a molar ratio of 8:2, and the mixture was stirred for 15 minutes. DMAEMA was subsequently added in a molar ratio of (MAPTMS:ZPO):DMAEMA = 9:1. In the final stage, 4,4'-bis(diethylamino) benzophenone (Michler's ketone, Sigma-Aldrich, Germany) was incorporated as the photoinitiator, at a concentration of 1% w/w relative to the monomers. After an additional 15 minutes of stirring, the composite was filtered using a 0.22 µm pore size syringe filter.

Prior to drop-casting of the photoresist on processed coverslips, the photoresist (2 mL) underwent a 4-hour vacuum treatment to enhance its viscosity, ensuring the droplet height matched the target heights (150 µm) for the 3D microstructure. After drop-casting was performed on processed coverslips, the samples were kept in a high vacuum environment for five days, ensuring the complete evaporation of any residual solvent.

After MPL the sample was immersed in 4-methyl-2-pentanone (Sigma-Aldrich, Germany) for 45 minutes to remove any unexposed material. Subsequently, the sample was immersed in isopropanol (Sigma-Aldrich, Germany) for 30 minutes to clean the glass substrate.

Experimental setup for the fabrication and characterization of 3D micro-devices

The experimental setups used to process and characterize 3D micro-devices are illustrated in Fig. S1. The micro-holes were processed into coverslips (Gerhard Menzel GmbH, Germany) with a diameter of 12 mm and a thickness of 130 μm using a Ti:Sa laser (Spitfire Ace, Spectra-Physics, United States). The laser emitted femtosesond (fs) laser radiation at 800 nm had an average output power of 2 W. The pulse width of the laser system was 110 fs, and the repetition rate was 5 kHz. For coverslip processing, the 8.3 mm ($1/e^2$) Gaussian raw beam ($M^2 = 1.11$) was transformed into a Bessel beam using an axicon (AX255-B, Thorlabs, United States) with an axicon angle α of 5°. The resulting Bessel beam was demagnified by a subsequent telescope objective consisting of two convex lenses ($f_1 = 160$ mm, $f_2 = 20$ mm) placed in the far field behind the axicon. The sample was positioned at the focus of the secondary Bessel zone behind the last lens, which is characterized by a calculated cone angle β of 17.7°, a focus depth of 1.6 mm, and a central core diameter ($1/e^2$) of 1.4 μm. The micro-hole was processed by moving the sample using an xyz-stage (M-521.DD for the x-axis and z-axis, M-511.DG for the y-axis, Physik Instrumente, Germany).

MPL was conducted using an ultrashort pulsed laser system (FemtoFiber ultra 780, Toptica Photonics AG) that emitted laser radiation with a central wavelength of 780 nm, a pulse duration of 150 fs, and a repetition rate of 80 MHz. To focus the laser beam into the photosensitive material, we used a microscope objective (20x/NA 0.8, Plan-Apo, Zeiss, Germany). A 2D galvo scanner (hurryscan II 10, Scanlab, Germany) and a shutter (MTS40-A3-750.850, AA Opto Electronics, France) were employed to produce each layer with its specific geometry. The performance of the galvo scanning system was further enhanced by a lens system. This lens system, which includes a f-theta lens (S4LFT4065/094, Sill Optics GmbH, Germany), effectively increases the usable field-of-view of the microscope objective, as described in Ref.[4].

To process 3D microstructures on the modified coverslips, two additional linear stages (M-605.1DD, Physik Instrumente, Germany) were utilized to locate the position of the micro-hole. Once the position was determined, the sample was processed using a layer-by-layer approach. After each layer was completed, the sample was shifted along its vertical axis in the z-direction using a linear stage of the same model. The sample was illuminated using an LED and the processing could be monitored in real-time using a camera.

After MPL, the 3D micro-devices were analyzed for their ability to enhance lateral resolution using a custom-built Mirau-type Coherence Scanning Interferometer (MCSI). The MCSI setup included a halogen light source with a central wavelength of 600 nm, a camera (Orca Flash 2.8, Hamamatsu, Japan), a Mirau-type microscope objective (50x/NA 0.55 CF Plan, Nikon, Germany), and a microscope lens scanner (Pifoc P-721.CD, Physical Instruments, Germany) with a scanning range of 100 μm. The 3D micro-device was integrated into the MCSI using a manual micrometer stage. The sample, specifically an Ag-grating, was mounted on a piezo-controlled XYZ-axis linear stage (NanoMax 300, Thorlabs, United States) to achieve nanometer-precision height control relative to the micro-sphere processed on the modified coverslip.
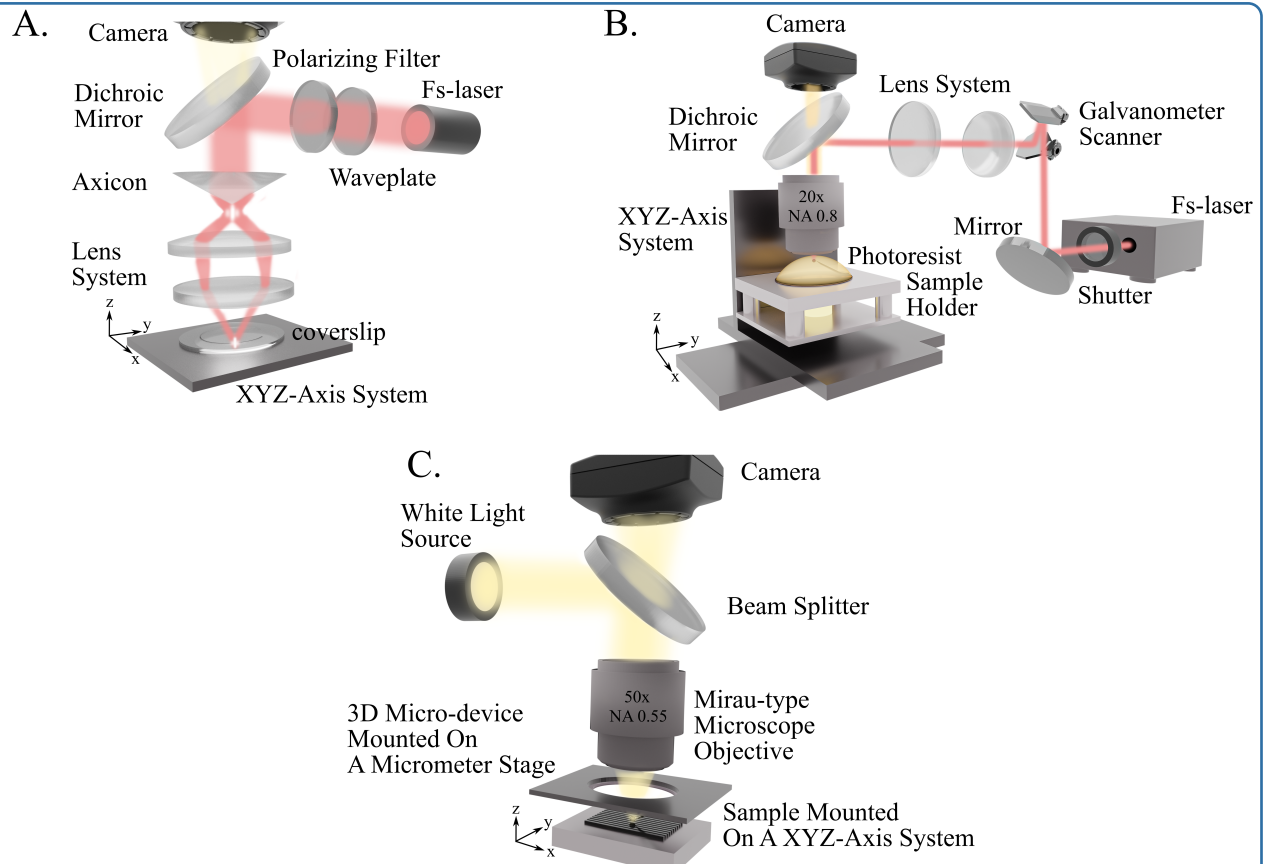
Fig. S1. Optical setups for manufacturing the 3D micro-device. (A) Optical setup for processing micro-holes into coverslips. (B) Optical setup for MPL. (C) Optical setup for MCSI

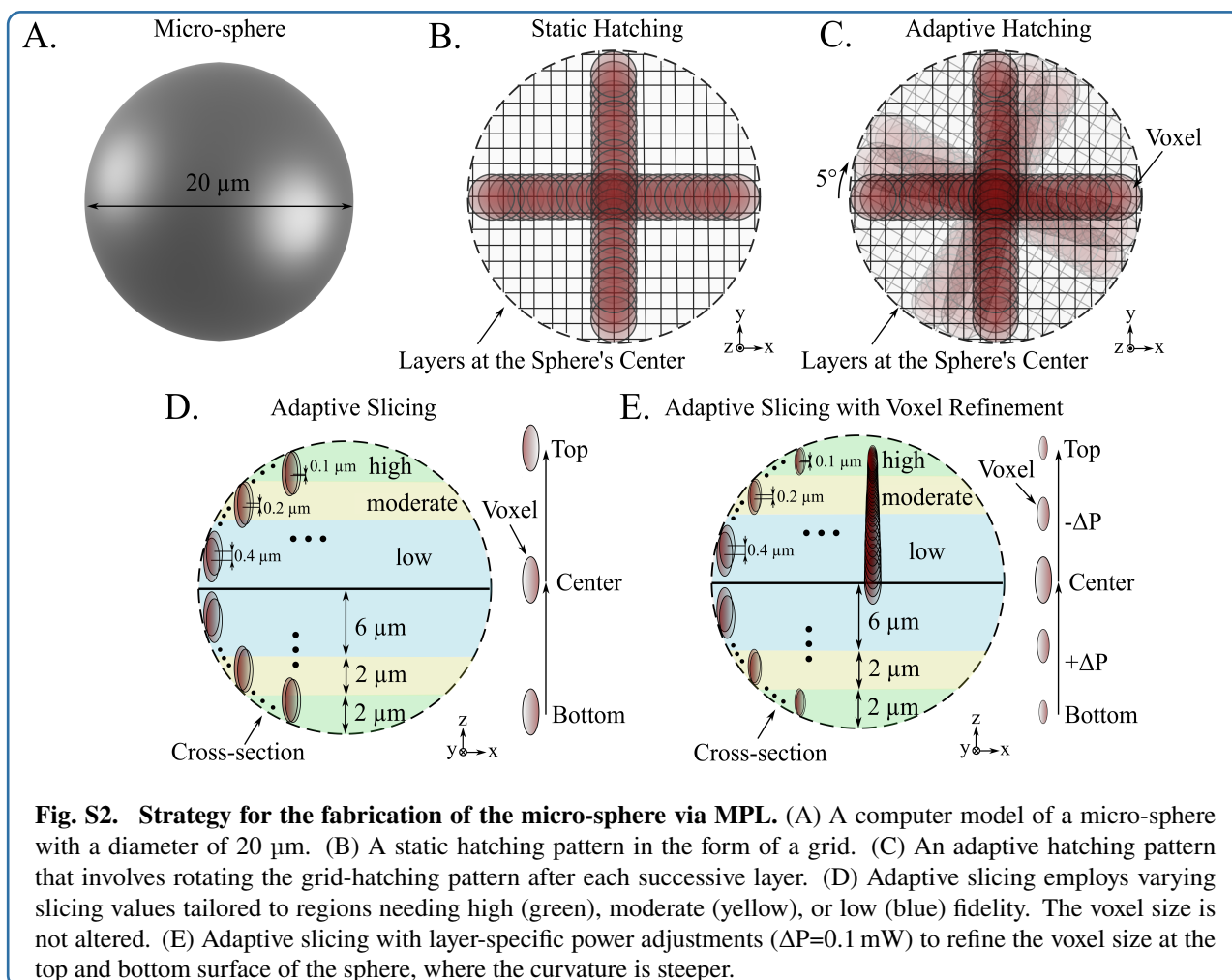## Effectiveness of adaptive hatching and slicing with layer-specific power adjustment for voxel refinement

Traditional MPL has proven effectiveness in accurately fabricating various structures with different geometries in a layer-by-layer manner utilizing computer designs that must be sliced into a specific number of layers, each hatched to define the laser's exposure paths. Nonetheless, MPL encounters challenges in fabricating high-quality structures with curved surfaces or spherical geometries, such as the micro-sphere proposed in this study (see Fig. S2A). These challenges primarily arise from static hatching and slicing strategies where hatching lines, typically forming a grid (see Fig. S2B), and layers are set at specific, yet constant distances, occasionally including the processing of each layer's contour. In combination with the inherent ellipsoidal shape of the voxel, such strategies are largely inadequate in accurately approximating curvatures or spherical structures. Moreover, the proximity and memory effects of photosensitive materials lead to polymerization volume growth, primarily along the vertical axis, when voxels overlap [5].

While each of the issues can generally be addressed using existing advanced MPL processing strategies, as detailed in Ref. [6], completely overcoming them remains a challenge, particularly in cases like the one presented in this study. Here, as explained in the main article, MPL cannot be conducted with oil-immersive microscope objectives with a numerical aperture of 1.4, which typically provides the optimal resolution for MPL. Consequently, fabricating the proposed micro-sphere with sufficient quality for optical applications necessitated further advancements in MPL processing strategies to mitigate all structural imperfections that would otherwise emerge, as will be detailed subsequently.

One such advancement is adaptive hatching, which, in the present study, utilized a standard grid-hatching pattern incrementally rotated by 5° clockwise with each subsequent layer (see Fig. S2C) to enhance the precision in approximating the circular geometry of each micro-sphere layer. To counteract polymerization volume growth along the vertical axis, the fabrication of the micro-sphere employed an adaptive slicing strategy. This strategy applied different slicing values, altering the voxel overlap by smartly defining regions based on their required fidelity, as illustrated in Fig. S2C. Ultimately, layer-specific power adjustments, conducted by an acousto-optic modulator, were included to refine the voxel size and enhance the overall fidelity when producing the bottom and top surfaces of the micro-sphere, where the curvature slope is steeper (see Fig. S2D).

A comprehensive comparison between standard and advanced MPL manufacturing strategies for fabricating the proposed micro-sphere is presented in the following with results specifically illustrated in Fig. S3 and Fig. S4. In this context, we will also explain the choice of specific parameters used to produce the final micro-sphere. This includes slicing values for the three regions requiring high, moderate, and low fidelity, as well as the average laser power values utilized. For all samples, the cantilever was consistently processed as described in the main article, employing an average power of 120 mW ($I = 1.44$ TW/cm^2) and a galvo speed of 30 mm/s. The fabrication parameters and strategies employed for each sphere are detailed in the respective subfigures.

Fig. S3 explicitly highlights the issues related to surface quality and roundness when viewing the micro-sphere from the top, alongside the successful mitigation of these issues through adaptive hatching. The micro-spheres depicted in Fig. S3A-C were fabricated with an increased distance between hatching lines to markedly emphasize the approximation of the circular shape of each layer through the standard hatching strategy. Concurrently, the resulting features of pixelated

Fig. S2. Strategy for the fabrication of the micro-sphere via MPL. (A) A computer model of a micro-sphere with a diameter of 20 μm. (B) A static hatching pattern in the form of a grid. (C) An adaptive hatching pattern that involves rotating the grid-hatching pattern after each successive layer. (D) Adaptive slicing employs varying slicing values tailored to regions needing high (green), moderate (yellow), or low (blue) fidelity. The voxel size is not altered. (E) Adaptive slicing with layer-specific power adjustments (ΔP=0.1 mW) to refine the voxel size at the top and bottom surface of the sphere, where the curvature is steeper.

structures closely aligns with the lateral voxel size of $d_v = 0.55$ μm estimated in the main article for an average power of P=47 mW ($I = 0.56$ TW/cm^2), thereby approximately validating the correctness of such calculations.

To enhance the precision of each layer's circular shape using standard MPL, the hatching parameter can be decreased, specifically to 0.1 μm in this study. Although incorporating contour processing is generally possible, it may significantly impact the surface quality of the micro-sphere. This occurs due to the exposure of certain regions to a second light incidence, typically increasing the polymerized volume in these areas (see Fig. S3D). However, in the absence of contour processing, a finer circular shape approximation achieved through reduced hatching distances resulted in improved roundness of the micro-sphere, especially when compared to those produced with a hatching distance of 0.4 μm (compare Fig. S3E-G with Fig. S3A-C). However, irrespective of the hatching precision, micro-spheres fabricated with larger slicing values tend to exhibit more pronounced surface roughness (compare Fig. S3B, C, F, and G). This phenomenon, often known as the staircase effect, arises from the discrepancy between slicing values and voxel dimensions in areas with shallow slopes, as highlighted in several past studies [7, 8, 9]. Notably, this error is not evident for micro-spheres sliced with 0.1 μm (see Fig. S3E).

A micro-sphere fabricated using only adaptive hatching, but not adaptive slicing, is depicted in Fig. S3H. It distinctly
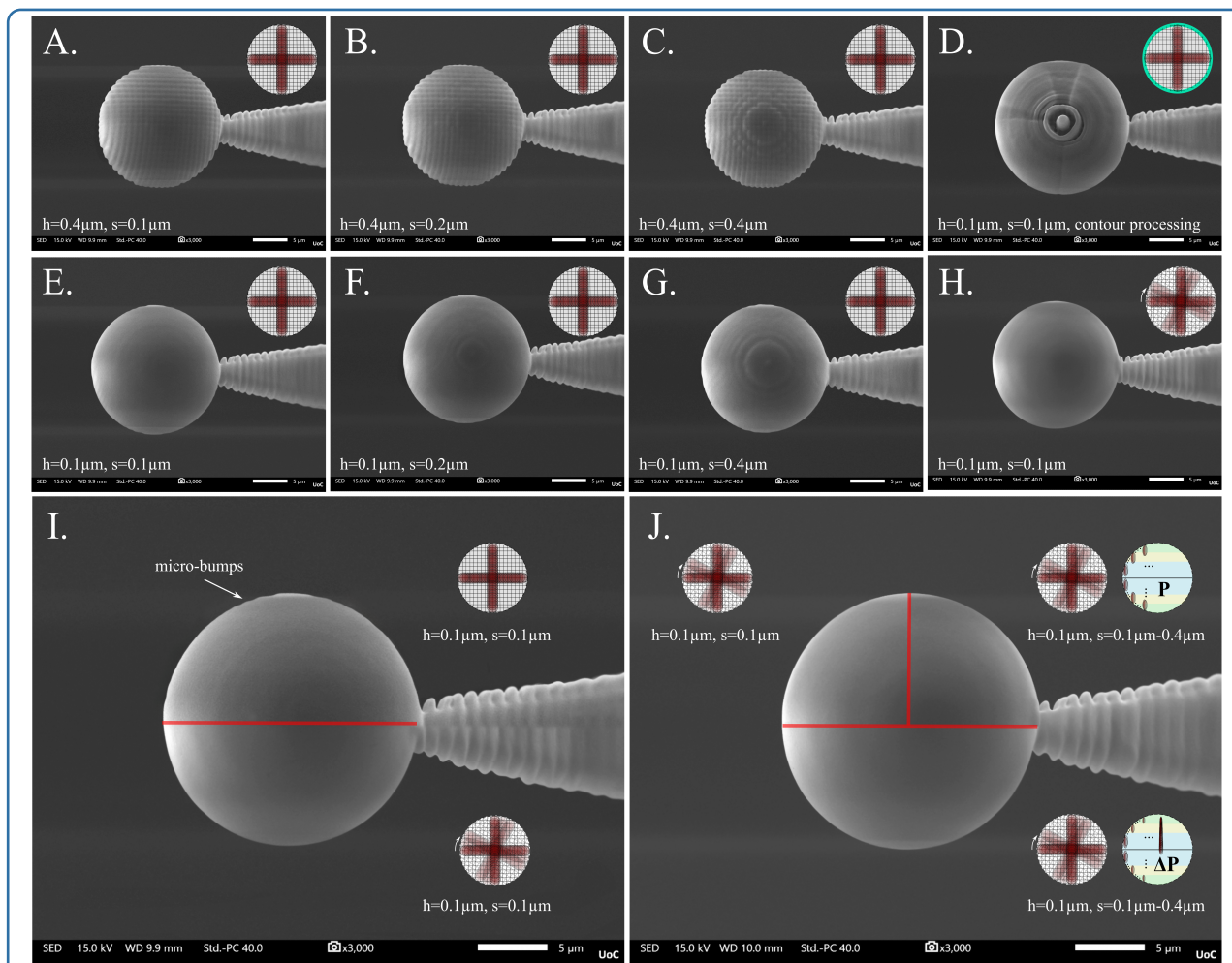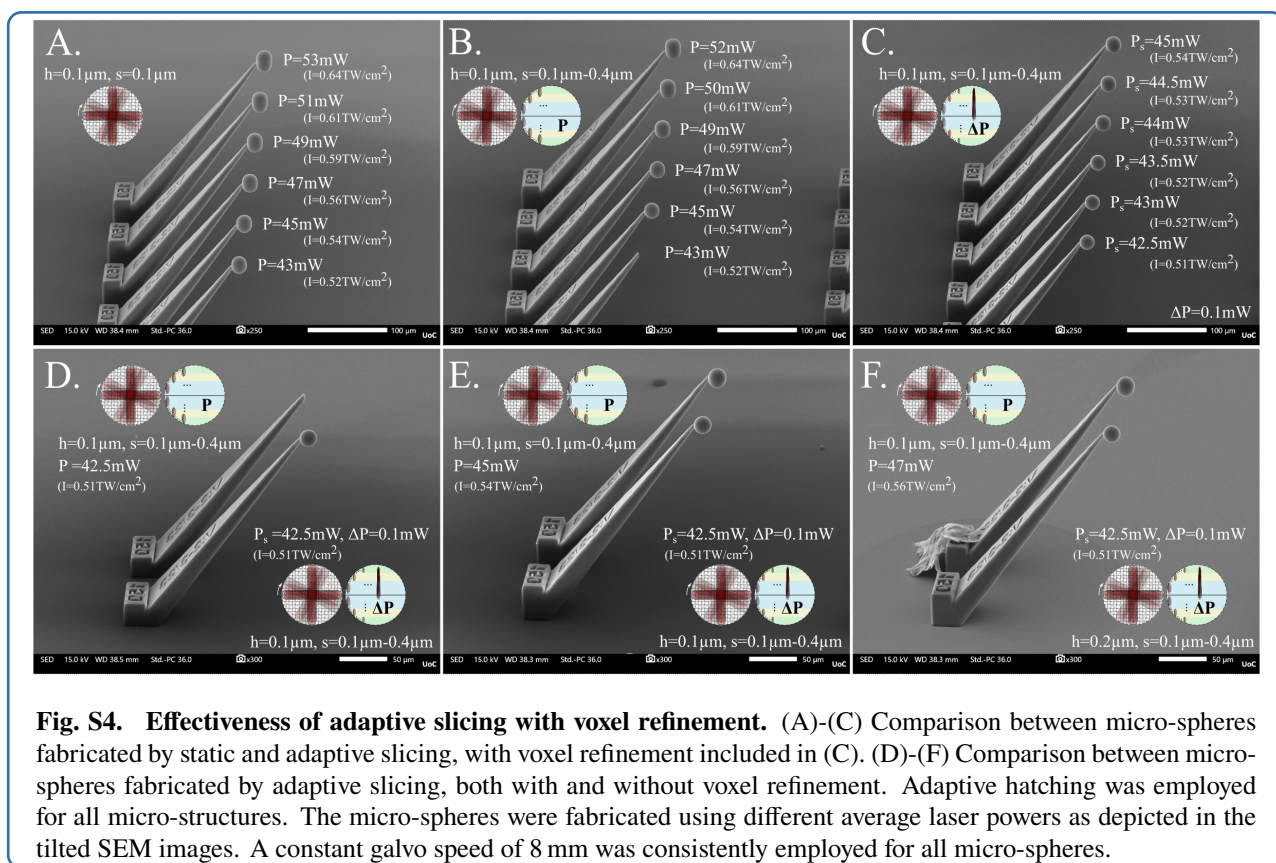
Fig. S3. Effectiveness of adaptive hatching. (A)-(H) All micro-spheres were fabricated using a static slicing strategy where layers are uniformly spaced, with parameters depicted in the corresponding SEM images. The micro-spheres shown in the top-view SEM images (A)-(G) were produced using static hatching, varying in hatching and slicing parameters. The micro-sphere in (D) underwent additional contour processing. (H) presents a top-view SEM image of a micro-sphere produced using adaptive hatching (I) Comparison between micro-spheres fabricated by static and adaptive hatching for identical fabrication parameters. The top-view SEM images are merged from two separately produced micro-spheres, specifically those depicted in (E) and (H). (J) Comparison between micro-spheres fabricated with and without adaptive slicing, while using the same parameters for adaptive hatching. In one instance of adaptive slicing, layer-specific power adjustments were applied for voxel refinement. The top-view SEM images are merged from three separately produced micro-spheres. The slicing employed in adaptive slicing is detailed in Fig. S2. The indicator P denotes adaptive slicing without voxel refinement, while ΔP indicates power adjustments detailed Fig. S2. The micro-sphere in (I) employing adaptive slicing with voxel refinement was fabricated using a starting average laser power of 42.5 mW ($I = 0.51$ TW/cm^2), as detailed in Fig. S4D-E and a galvo speed of 8 mm/s. All other micro-spheres were produced with an average laser power of 47 mW ($I = 0.56$ TW/cm^2) and a galvo speed of 8 mm/s.

demonstrates superior surface quality and roundness, even exceeding that of the micro-sphere fabricated by standard MPL with identical hatching and slicing parameters, particularly as observed in an enlarged subfigure (see Fig. S3I). In this example, the micro-sphere fabricated by traditional MPL exhibited numerous small micro-bumps along its contour, whereas the one produced through adaptive hatching is notably smoother. These micro-bumps are suggested to result from the static application of the grid-hatching pattern in traditional MPL, which provides only a limited approximation of the circular geometry of each layer. This limitation persists even when the hatching parameter is reduced. In contrast, adaptive hatching refines this approximation by dynamically rotating the grid pattern after each layer, achieving a more uniform and circular geometry in each layer and thereby higher fidelity compared to traditional MPL. Consequently, adaptive hatching substantially improves both the roundness viewed from the top and the overall surface quality of the micro-sphere, as clearly demonstrated in Fig. S3I.

Interestingly, when adaptive hatching is combined with adaptive slicing — with or without layer-specific power adjustments — the surface quality and roundness of the sphere, when viewed from the top, seem unaffected by the advanced slicing strategy (see Fig. S3J). Notably, in employing advanced slicing, measures were taken to counteract the staircase effect by establishing three regions of high, moderate, and low fidelity in the fabrication process of the micro-sphere. The sizes of these regions were determined based on the intensity of surface defects observed at the top part of previously studied micro-spheres (see Fig. S3E-G), while concurrently aiming to minimize the number of layers and counteract the volumetric growth of polymerization along the vertical axis. Therefore, the fidelity regions were parameterized for one half of the micro-sphere with s=0.1 μm for 2 μm (high fidelity - green), s=0.2 μm for 2 μm (moderate fidelity - yellow), and s=0.4 μm for 6 μm (low fidelity - blue) and then mirrored for the other half of the micro-sphere. Additional parameters selected for adaptive slicing with power modifications will be elaborated upon.

To demonstrate the effectiveness of adaptive slicing, with or without layer-specific power adjustments, a comparison between the micro-spheres produced using adaptive hatching with standard slicing and adaptive slicing is presented in the following. Fig. S4A vividly illustrates that static slicing leads to structural distortions in the intended spherical design, primarily manifesting as axial elongation. As aforementioned, this elongation results from the overlapping of identical voxels, which promotes specific polymerization growth. The degree of elongation depends on the average laser power used to produce the micro-sphere. Additionally, as the laser power increases, the micro-spheres tend to expand laterally, especially near the top and bottom, due to increased voxel size that limits the accuracy in fabricating such parts of the micro-sphere requiring high fidelity.

In contrast, adaptive slicing yielded superior results compared to static slicing under the same average laser power settings, even without layer-specific power adjustments (see Fig. S4B). The reduced axial elongation of the micro-spheres results from the modified voxel overlap across three different sliced regions along the micro-sphere's volume, coupled with a reduced number of layers used to produce the micro-spheres compared to the ones illustrated in Fig. S4A. Such adjustments effectively diminish the polymerization growth in the axial direction to a certain extent. The most refined micro-sphere produced by adaptive slicing, without layer-specific power adjustments, was achieved at an average laser power of 45 mW. However, upon closer examination, this micro-sphere exhibited axial elongation and lateral expansion near the top and bottom surfaces. These minor imperfections might potentially be mitigated by further reducing the

Fig. S4. Effectiveness of adaptive slicing with voxel refinement. (A)-(C) Comparison between micro-spheres fabricated by static and adaptive slicing, with voxel refinement included in (C). (D)-(F) Comparison between micro-spheres fabricated by adaptive slicing, both with and without voxel refinement. Adaptive hatching was employed for all micro-structures. The micro-spheres were fabricated using different average laser powers as depicted in the tilted SEM images. A constant galvo speed of 8 mm was consistently employed for all micro-spheres.

laser power, targeting the well-curved bottom and top surfaces observed in the micro-sphere fabricated using standard slicing at an average laser power of $43\,\text{mW}$ ($I = 0.52\,\text{TW/cm}^2$)(see Fig. S4A). However, due to the enhanced slicing parameters, decreasing the laser power in adaptive slicing did not ensure a stable connection between the cantilever and the micro-sphere, impacting its removal during the development process when solving any unexposed material.
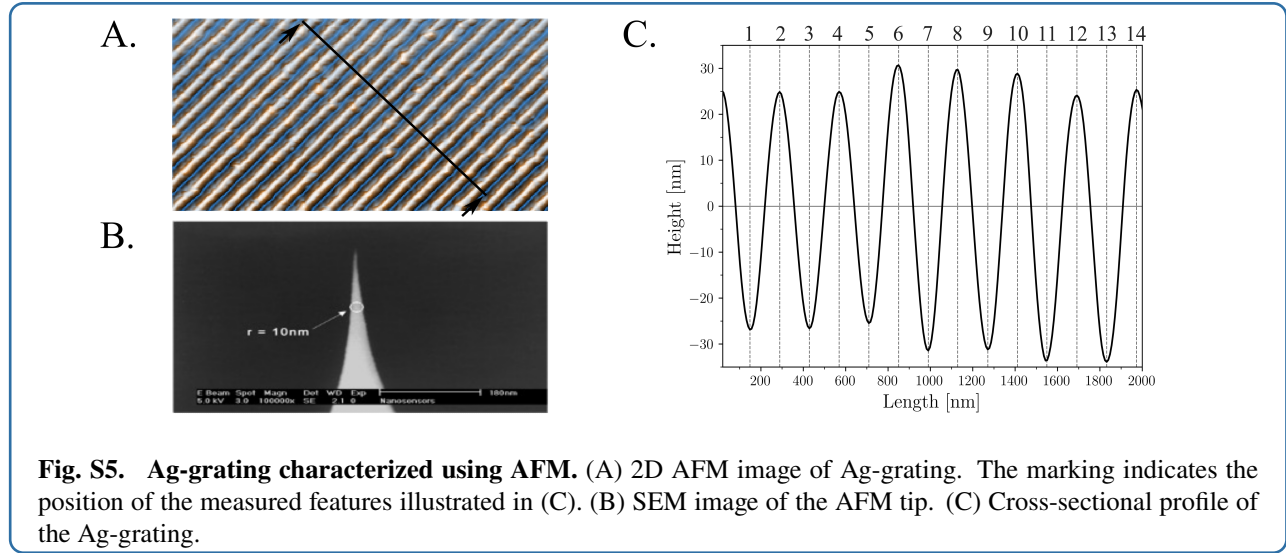
The key factor in further refining the spherical geometry of the micro-sphere was the utilization of adaptive slicing in combination with layer-specific power adjustments. This approach enabled a precise approximation of the micro-sphere's geometry, particularly at the bottom and top surfaces, while simultaneously ensuring a stable connection of the structure to the cantilever (see Fig. S4C). The selection of the initial value for the average laser power (P_s) and the variation in laser power (ΔP) were determined under consideration of findings achieved in this study and other aspects. These aspects included the number of layers defined to process the micro-sphere, average power values to ensure well-curved bottom and top surfaces of the micro-sphere, and those that ensure a stable connection of the micro-sphere to the cantilever, as well as considering the technical limitations of the MPL system. Notably, the laser power was continuously adjusted throughout the entire fabrication process to ensure a smooth transition between the three regions in terms of polymerized volume.

Ultimately, the use of adaptive hatching, in conjunction with adaptive slicing and layer-specific power adjustments, enabled the fabrication of an almost perfect micro-sphere. Specifically, the optimal micro-sphere was fabricated starting with an average laser power of Ps=$42.5\,\text{mW}$ ($I = 0.51\,\text{TW/cm}^2$) at the bottom, incrementally increased by ΔP=$0.1\,\text{mW}$, peaking at $47\,\text{mW}$ ($I = 0.56\,\text{TW/cm}^2$) for the sphere's central layer, before decreasing to $42.5\,\text{mW}$ ($I = 0.51\,\text{TW/cm}^2$) by

the same incremental value when approaching the processing at the top surface of the structure. As evident in Fig. S4C-F, this advanced MPL strategy is not only effective in producing an almost perfect micro-sphere but it is also highly reproducible.

Characterization of Ag-grating using atomic force microscopy

To test the optical properties of the 3D micro-device, a calibration grating (TDG01, TipsNano, Estonia) served as a sample (see Fig. S5A). This grating is an Ag-grating formed on chalcogenide glass with a period of Λ=0.28 µm and a height h greater than 50 nm. Prior to MCSI, the grating's features were analyzed using atomic force microscopy (AFM, NX20, Park System, Korea). AFM measurements were conducted in non-contact mode, employing a high-resolution non-contact cantilever (SSS NCHR 10M, Nanosensors^{TM}, Switzerland) (see Fig. S5B). A profile of the grating, measured by AFM at an arbitrarily selected area, is displayed in Fig. S5C. The profile was smoothed using Savitzky-Golay filter[10].

Fig. S5. Ag-grating characterized using AFM. (A) 2D AFM image of Ag-grating. The marking indicates the position of the measured features illustrated in (C). (B) SEM image of the AFM tip. (C) Cross-sectional profile of the Ag-grating.

Furthermore, the period of the grating Λ and the height h were determined using the measured profile. The measured distances and height difference between each data point are listed in Tab. 1. The average period and height of the grating can be calculated to be Λ=0.28 µm $\pm$ 0.001 µm and h=57 nm $\pm$ 5 nm, respectively. These calculated values align well with the grating's specifications.

Table 1: Measured distance and height difference between single features of the Ag-grating.

Data	1-2	2-3	3-4	4-5	5-6	6-7	7-8	8-9	9-10	10-11	11-12	12-13	13-14
Distance [nm]	140.4	139.9	140.8	140.2	140.3	140.3	138.5	142.4	140.2	138.3	142.0	140.7	140.6
Height [nm]	51.6	50.9	50.9	50.2	55.9	61.8	61.0	60.8	60.0	62.3	57.6	57.9	59.1

3D micro-devices with elongated micro-spheres

As described in the main file, the exposure paths of micro-sphere had to be defined through an approach that is established as hatching and slicing. In this case, the same hatching a slicing strategy was employed as described in the main file.
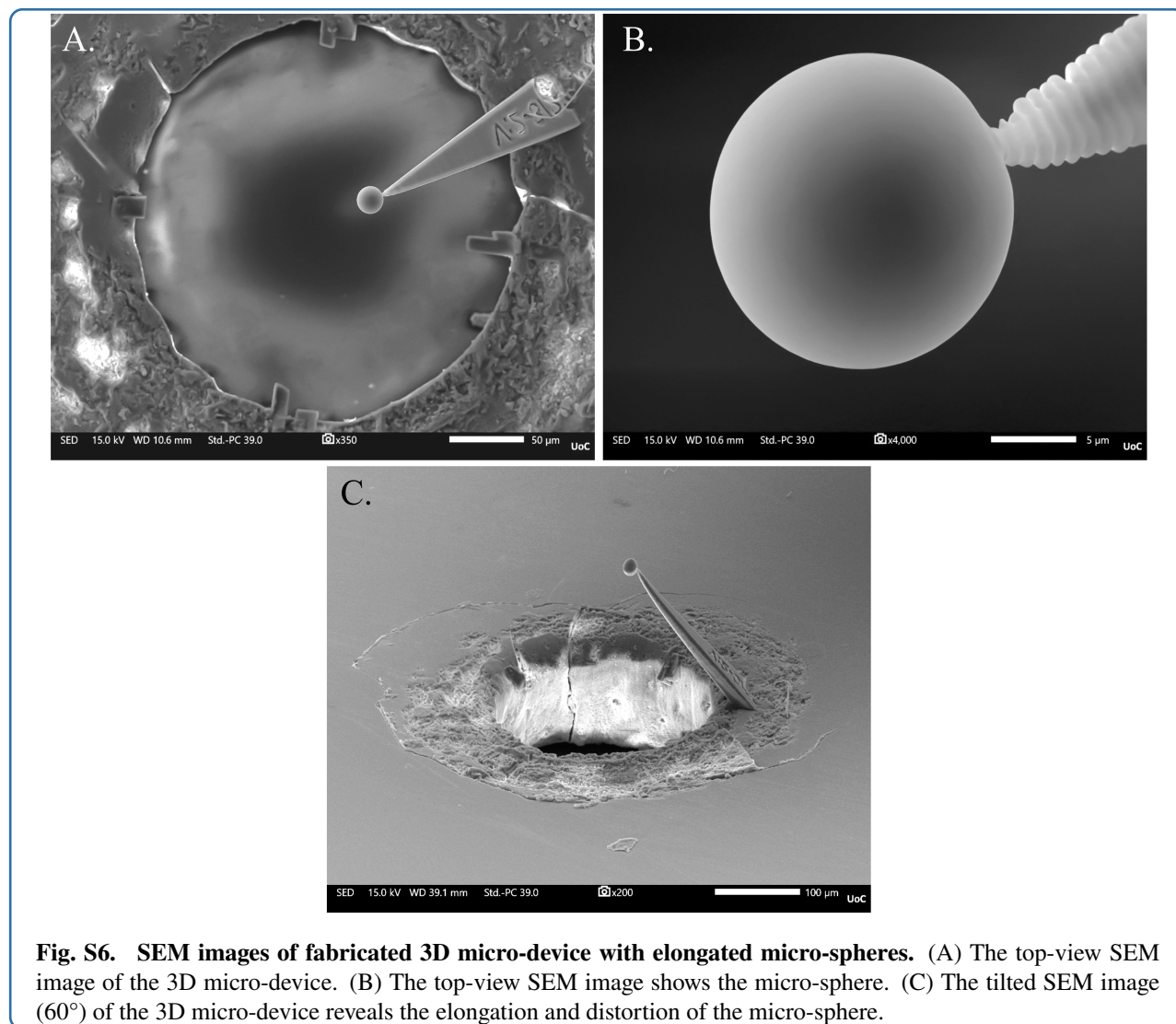

Fig. S6. SEM images of fabricated 3D micro-device with elongated micro-spheres. (A) The top-view SEM image of the 3D micro-device. (B) The top-view SEM image shows the micro-sphere. (C) The tilted SEM image (60°) of the 3D micro-device reveals the elongation and distortion of the micro-sphere.

Hatching lines were spaced at an interval of 0.1 µm. The grid pattern was rotated by 5° clockwise for each successive layer. Slicing for this micro-sphere alternated between 0.1 µm, 0.2 µm, and 0.4 µm. However, in this case, the procedure referred to as "adaptive slicing" did not incorporate layer-specific power adjustments. The micro-sphere was processed with a consistent average laser power of 47 mW ($I = 0.56$ TW/cm^2). The galvo speed was 8 mm/s and the cantilever was processed as described in the main file. The result of this process is presented in Fig. S6. The SEM images further validate that the adaptive hatching technique results in a noticeably smooth surface (see Fig. S6A,B). However, Fig. S6C clearly shows the elongation and distortion of the structure identified as a micro-sphere. This elongation was caused by the overlapping voxels as described before [8, 5].
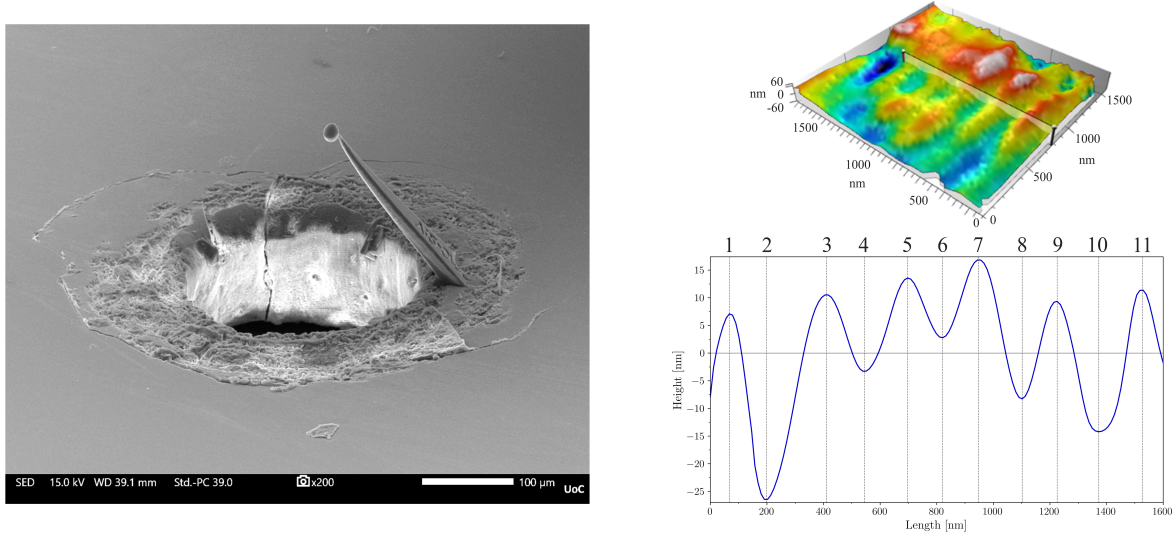
Fig. S7. **Characterization of a 3D micro-device with non-perfect micro-sphere for lateral resolution enhancement using MCSI.** The tilted image (60°) on the left-hand side shows the 3D microstructure with the elongated micro-sphere. The image and graph on the right-hand side show the result of micro-sphere-assisted MCSI and the cross-sectional profile of the Ag-grating measured by the 3D micro-device using MCSI, respectively.

Nevertheless, this 3D micro-device was tested for its potential to enhance lateral resolution using MCSI. Interestingly, an enhancement in lateral resolution could be achieved, enabling to resolve an image with features of the Ag-grating (see Fig. S7). This would not have been possible using only the Mirau-type microscope, which has a resolving power of 0.5 µm. However, the grating's period (Λ=0.28 µm) and height ($h > 50$ nm) could be determined less accurately compared to the almost perfect micro-sphere presented in the main article. Using the micro-sphere presented in Fig. S7, the average values for the grating's period and height were calculated to be Λ=0.29 µm $\pm$ 0.032 µm and h=18.3 nm $\pm$ 5.1 nm, respectively. Such values were determined using the profile measured by MCSI with the 3D micro-device (see Fig. S7). The profile was smoothed using Savitzky-Golay filter[10]. The distances and height differences between individual features of the Ag-grating, as measured by the 3D micro-device using MCSI, are listed in detail in Tab. 2. As discussed in the main article, the primary reasons for the inaccuracy in the measurement are likely the elongated and distorted shape of the structure, which could cause alterations in both the optical path length and the focal distance.

Table 2: Measured distance and height difference between single features of the Ag-grating.

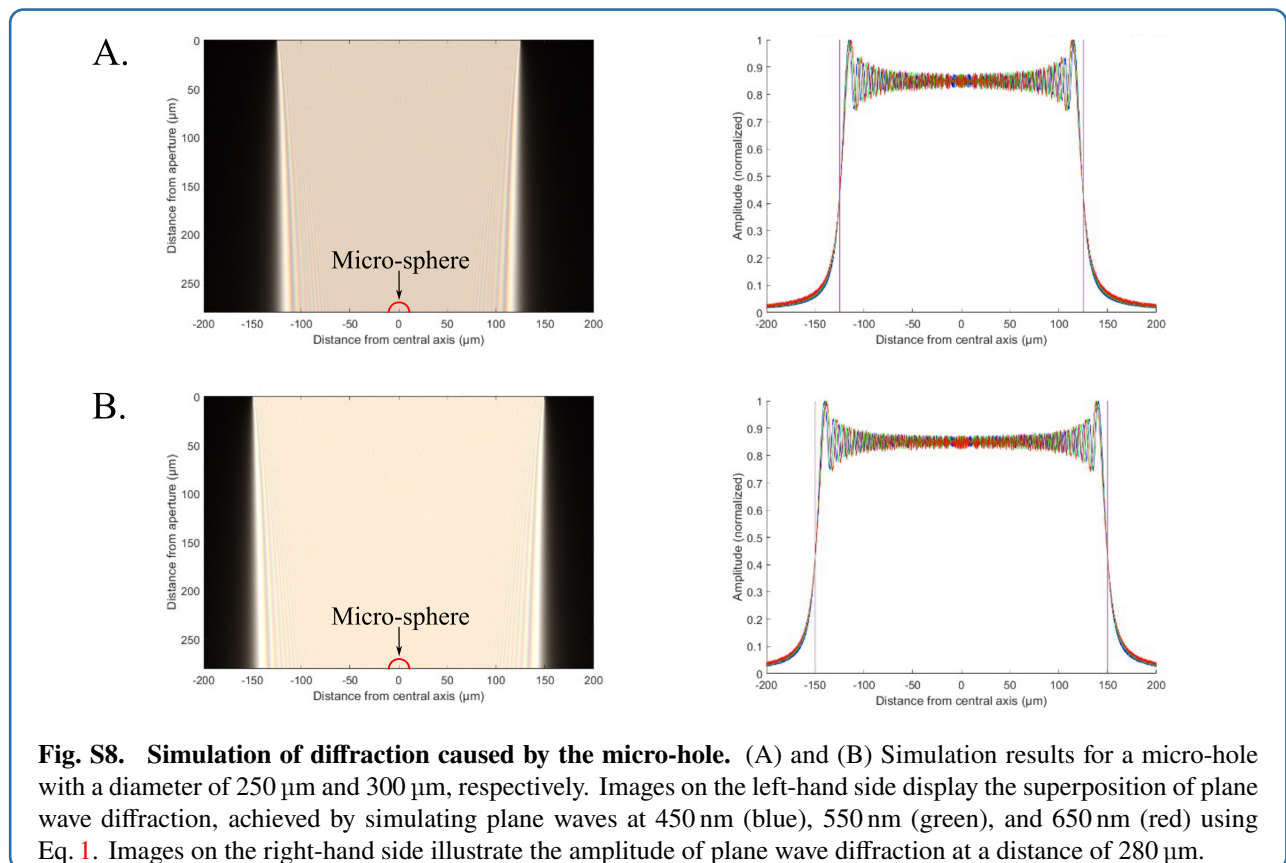| Data	1-2	2-3	3-4	4-5	5-6	6-7	7-8	8-9	9-10	10-11
Distance [nm]	130.6	212.2	134.2	152.6	123.5	126.7	154.5	123.5	146.9	154.4
Height [nm]	19.4	15.9	13.8	16.9	10.83	14.1	25.2	17.7	23.6	25.6

Diffraction caused by the micro-hole

To investigate the diffraction effect caused by the micro-hole processed in the coverslip, simulations were conducted on the basis of Ref. [11] using the Huygens-Fresnel principle. In this approach, the plane wave propagating through the micro-hole was simulated as a sum of evenly spaced spherical waves. As the simulation is 2D, the attenuation factor is the inverse square root of the distance, which can be described as follows:

$$U(x, y) = A \sum_n \frac{1}{\sqrt{r_n}} e^{i(kr_n)}, \qquad r_n = \sqrt{(x - x_n)^2 + (y - y_n)^2},$$ (1)

where U represents the resulting wave amplitude, A the amplitude of each wave (assumed constant), k the wave number, and r_n the radius of the wave, with x_n and y_n denoting the locations of each point source.

Given that the micro-hole diameter ranges between 250 µm and 300 µm, the thickness of the coverslip is 130 µm, and the cantilever holds the microsphere at a height of 150 µm, simulations were conducted by propagating the waves out to a distance of 280 µm. In this context, three plane waves with wavelengths of 450 nm, 550 nm, and 650 nm were simulated, representing white light illumination. The spacing between the point sources was set at 100 nm.

Fig. S8. Simulation of diffraction caused by the micro-hole. (A) and (B) Simulation results for a micro-hole with a diameter of 250 µm and 300 µm, respectively. Images on the left-hand side display the superposition of plane wave diffraction, achieved by simulating plane waves at 450 nm (blue), 550 nm (green), and 650 nm (red) using Eq. 1. Images on the right-hand side illustrate the amplitude of plane wave diffraction at a distance of 280 µm.

The results are demonstrated in Fig. S8 and show that the diffraction effects from the edges of the micro-hole are negligible within the region of the micro-sphere, even when the structure's position is slightly misaligned relative to the center of the micro-hole. Only a base level of highly frequency-dependent noise remains. Thus, it can be concluded that

the diffraction effects close to the micro-sphere are minimal and may not significantly impact the imaging properties. They only slightly reduce the signal-to-noise ratio.

References

[1] Ovsianikov, A. et al. Ultra-Low shrinkage hybrid photosensitive material for two-photon polymerization microfabrication. *ACS Nano* **2**, 2257–2262 (2008).

[2] Ladika, D. et al. Synthesis and application of triphenylamine-based aldehydes as photo-initiators for multi-photon lithography. *Applied Physics A* **128**, 745 (2022).

[3] Sakellari, I. et al. Diffusion-assisted high-resolution direct femtosecond laser writing. *ACS Nano* **6**, 2302–2311 (2012).

[4] Bumstead, J. R. et al. Designing a large field-of-view two-photon microscope using optical invariant analysis. *Neurophotonics* **5**, 025001 (2018).

[5] Fischer, J. & Wegener, M. Three-dimensional optical laser lithography beyond the diffraction limit. *Laser & Photonics Reviews* **7**, 22–44 (2013).

[6] Gonzalez-Hernandez, D. et al. Micro-optics 3D printed via multi-photon laser lithography. *Advanced Optical Materials* **11**, 2201701 (2023).

[7] Park, S. H. et al. Subregional slicing method to increase three-dimensional nanofabrication efficiency in two-photon polymerization. *Applied Physics Letters* **87**, 154108 (2005).

[8] Zhou, X. Q., Hou, Y. H. & Lin, J. Q. A review on the processing accuracy of two-photon polymerization. *AIP Advances* **5**, 030701 (2015).

[9] Guo, R. et al. Micro lens fabrication by means of femtosecond two photon photopolymerization. *Optics Express* **14**, 810–816 (2006).

[10] Savitzky, A. & Golay, M. J. E. Smoothing and differentiation of data by simplified least squares procedures. *Analytical Chemistry* **36**, 1627–1639 (1964).

[11] Mahan, J. et al. Monte carlo ray-trace diffraction based on the huygens–fresnel principle. *Applied Optics* **57**, D56–D62 (2018).